

Effects of Roughness on Reflection of Monochromatic Light

Spencer Thevenin

A senior thesis submitted to the faculty of
Brigham Young University
in partial fulfillment of the requirements for the degree of

Bachelor of Science

Steve Turley, Advisor

Department of Physics and Astronomy

Brigham Young University

April 2017

Copyright © 2017 Spencer Thevenin

All Rights Reserved

ABSTRACT

Effects of Roughness on Reflection of Monochromatic Light

Spencer Thevenin

Department of Physics and Astronomy, BYU

Bachelor of Science

If the scale of surface roughness is on the order of the wavelength of incident light, traditional optics methods like ray tracing and physical optics fail to adequately model reflectance. In this project, boundary integral techniques were chosen because they provide direct solutions only limited by computer memory. Discretizing Maxwell's equations across a surface yields an $Ax = b$ matrix equation relating the surface current to electric field over a net of points. Reflectance calculations for transverse-magnetic (TM) waves on a perfect conductor in two dimensions are analyzed in depth to model the effects of scattering from surface roughness. Root mean square (rms) surface roughness more than a hundredth the wavelength of the incident beam is noticeable and anything larger than a tenth the wavelength dominates the reflectance. These calculations allow for comparison with previous approaches –such as the scalar correction factors of Debye-Waller – at various spatial frequencies. The Debye-Waller models the smaller roughness but loses precision as roughness increases. The effects of spatial frequencies are also analyzed and compared to the current work of Stearn in showing additional surface parameters affecting roughness. The results of altering spatial frequency supports the work of Stearn suggesting additional parameters like spatial frequency are factors that affect overall reflectance. Optimizing the calculation through generating and solving the matrix equation are analyzed. Nonsingular, off-diagonal elements of the relation matrix are relatively slow to calculate in the generation process. A method using the multipole expansion is theorized to combat this inefficiency.

Keywords: [XUV, EUV, Monochromatic, Reflectance, Mirror, Roughness, Debye, Waller, Debye-Waller]

ACKNOWLEDGMENTS

I would like to thank Dr. Turley first and foremost for presenting this idea to me and having the confidence in my ability to complete such a task. I am grateful for all the hours he put in in explaining, revising, and question answering throughout the whole process. I also want to thank my wife for the countless hours of listening to me, staying late in the lab, and providing light and optimism during the discouraging parts of this project. I want to thank my research group who have provided endless feedback from presentation to papers. Lastly, I want to thank the BYU Physics Department as well as all those involved in the Edwin G. Wooley Mentorship for all the funding and resources they have provided me in my research.

Contents

Table of Contents	iv
List of Figures	1
1 Introduction	3
1.1 XUV Mirrors	3
1.2 Prior Work	5
1.3 Maxwell Equations and the Wave Equation	6
1.4 Green's Function	8
1.5 Perfect Conductor	8
1.6 Matrix Equation	9
1.7 Scope of Project	11
2 Numerical Methods/Setup	12
2.1 Incident Wave	12
2.2 Surface Discretization	14
2.2.1 Quadrature Rules	14
2.2.2 Handling Singularities	17
2.3 Path Integrals	18
2.4 Generating the Matrix	18
2.5 Surface Generation	19
2.6 Solving the Matrix Equation	24
2.7 Far-Field Calculation	26
3 Results	28
3.1 Effects of surface roughness	28
3.1.1 rms Roughness	29
3.1.2 Spatial Frequency	31
3.2 Optimization	32
3.3 Direct vs iterative	32
3.4 Fill vs solve	33

4	Conclusions and future work	35
4.1	Roughness threshold	35
4.2	Comparison to Debye-Waller	36
4.3	Spatial frequency implications	38
4.4	Multipole expansion	39
	Bibliography	42

List of Figures

1.1	Setup of correction factors	5
2.1	Setup of incident beam, outgoing spherical wave, and surface current Diagram . . .	13
2.2	Origin of coordinates	14
2.3	Quadrature rules	15
2.4	Nystrom discretized surface	16
2.5	Flat and linear surface	20
2.6	Rms roughness on surface generation	20
2.7	Surface generation of different spatial frequencies	21
2.8	Surface generation of different spatial frequencies	22
2.9	Surface generation of different spatial frequencies	23
2.10	Flat far-field	27
3.1	Effects of rms roughness	29
3.2	Extreme effects of rms roughness	30
3.3	Reflection effects from differing spatial frequencies	31
3.4	Logarithmic plot of Direct vs Iterative solvers	33
4.1	Comparison of results and Debye-Waller correction	37
4.2	Reflectance from different spatial frequencies	38

4.3 Chart of multipole expansion 40

Chapter 1

Introduction

Understanding the extreme ultraviolet (XUV) has been a major part of recent optical studies. One of these studies is developing mirrors to effectively reflect XUV light. Using XUV in reflectance present new challenges. These challenges are overcome through using Maxwell's equation to generate the Helmholtz equation. Helmholtz equation allow us to solve for a Green's function which provides the relationship between the incident light and the current induced on the mirror during the reflection process. The surface currents are solved by forming a matrix equation of the Green's function. The background behind the derivation are given in this chapter to prepare us for further analysis in later chapters.

1.1 XUV Mirrors

In recent years, technology and innovation have extended the limits in the field of optics through the use of the extreme ultraviolet (XUV). XUV is a region within the electromagnetic spectrum between 120 and 10 nm. With shorter wavelengths and greater energy, XUV enhances capacity and scope of many optical instruments. XUV has improved the precision of a recently developed desktop microscope created from a compact laser-plasma [1]. This microscope has provided better

resolution and detail than similar microscopes using lower energies. Improved performance was also found in XUV contact-hole printing [2]. Due to smaller wavelengths there was improved control and faster etching.

In recent years, NASA has been interested in improving their telescopes to detect and utilize XUV light. This ability would improve the imaging and detection of stars as well as provide enhanced analysis of their composition. The telescopes contain mirrors that are vital to control, reflect, and magnify incoming and outgoing light. The Turley-Allred XUV research group has been working on developing mirrors that meet this criteria. The group has made progress towards this goal but have run into a few challenges along the way. One of these problems arises from the inability to create a perfectly smooth surface.

The smaller wavelengths of XUV present problems in calculating reflectance. The wavelengths of XUV light approach the size of the roughness on the surface of the mirror. The resulting scattering of the light is less obvious and more unpredictable. This better understood through an analogy.

The effects of scattering from a rough surface is contrasted to bouncing a ball on the ground. Suppose you are holding a basketball and the ground you are dribbling the ball on is a bed of rocks the size of ping-pong balls. The rocks will have a minimal effect of the trajectory of the ball because the ball is much bigger than the bed of rocks. Now, as the size of the ball decreases predicting the trajectory of the ball is much harder. Taking a bouncy ball the size of a ping-pong ball and bouncing it off the bed of rocks yields more complicated to predict trajectories. This complication is similarly found in waves and surface roughness.

Traditional methods found in most books, like ray tracing and physical optics, fall short in effectively modeling the reflectance from these surface features because they assume the wavelength is much larger than the roughness on the surface. Many mirrors that are effective at reflecting visible and softer ultraviolet light are nearly invisible to XUV due to the shorter wavelengths of XUV light because the waves pass right through. Recent studies have been undergone to understand

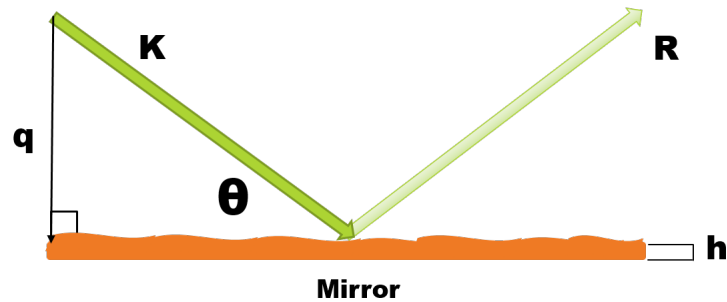


Figure 1.1 Depiction of the setup used for correction factors. For the specific case of Debye-Waller, k is the wavevector of the incoming beam, q is the momentum of the incident beam perpendicular to the mirror, θ is the grazing angle, and h is the rms high of the roughness, and R is the reflectance of the scatter wave.

reflectance properties in the XUV from surface roughness.

1.2 Prior Work

Different methods for dealing with roughness have been studied. Scalar correction factors have recently been formulated as a method to correct for roughness on the surface. The two most well-known of these corrections are the Debye-Waller and Nevot-Croce factors. [3,4]

Scalar correction factors are the most common way to handle surface factors. Scalar correction factors are modeled by [5,6]:

$$R = R_0 C \quad (1.1)$$

where R is the reflected intensity, R_0 is the calculated reflected intensity off a flat surface, and C is the correction factor. Correction factors of this nature are created from a myriad of things: rms

roughness height, from the surface, h , the angle of the incident beam, θ , and material properties such as index of refraction. The most common of these are Debye-Waller (DW) and Nevot-Croce (NC). Debye-Waller is most applicable to this project and is given by:

$$R = R_0 e^{-4q^2 h^2}, \quad (1.2)$$

where q is the momentum perpendicular to the surface of the incident beam. (see Fig. 1.1) Substituting for the wavenumber, k , and grazing angle, q is given as

$$q = k \sin(\theta) \quad (1.3)$$

The DW factor uses the wavenumber, incident beam, and rms roughness to correct for the roughness. However, to fully model how light interacts with the surface, these approximations prove insufficient.

Jedidiah Johnson's Master's Thesis [7] outlines these deficiencies and proposes that a direct solution with minimal approximation will improve reflectance calculations from surface roughness. Johnson's method provides a direct solution through Maxwell Equations.

1.3 Maxwell Equations and the Wave Equation

The well known Maxwell Equations provide the foundation of electromagnetism. They are given by

$$\nabla \cdot \mathbf{E} = \frac{\rho}{\epsilon_0}, \quad (1.4)$$

$$\nabla \cdot \mathbf{B} = 0, \quad (1.5)$$

$$\nabla \times \mathbf{E} = -\frac{\partial \mathbf{B}}{\partial t}, \quad (1.6)$$

$$\nabla \times \mathbf{B} = \mu_0 \mathbf{J} + \mu_0 \epsilon_0 \frac{\partial \mathbf{E}}{\partial t}, \quad (1.7)$$

where E is the electric field, ρ is the charge density, ϵ_0 is the permittivity of free space, B is the magnetic field, t is time, μ_0 is the permeability of free space, and J is the current density.

From Maxwell's Equation the wave equation is derived. Taking the curl of Eq. 1.6 gives

$$\nabla \times (\nabla \times \mathbf{E}) + \frac{\partial}{\partial t} (\nabla \times \mathbf{B}) = 0. \quad (1.8)$$

Using Eq. 1.5, $\nabla \times \mathbf{B}$ from Eq. 1.8 is eliminated through substitution, giving

$$\nabla \times (\nabla \times \mathbf{E}) + \mu_0 \epsilon_0 \frac{\partial^2 \mathbf{E}}{\partial t^2} = -\mu_0 \frac{\partial \mathbf{J}}{\partial t}. \quad (1.9)$$

The vector identity, $\nabla \times (\nabla \times \mathbf{E}) = \nabla(\nabla \cdot \mathbf{E}) - \nabla^2 \mathbf{E}$, is applied and Eq. 1.4 replaces $\nabla \cdot \mathbf{E}$ which gives

$$\nabla^2 \mathbf{E} - \mu_0 \epsilon_0 \frac{\partial^2 \mathbf{E}}{\partial t^2} = -\mu_0 \frac{\partial \mathbf{J}}{\partial t} + \frac{\nabla \rho}{\epsilon_0}. \quad (1.10)$$

Removing all sources from the area of interest ($\rho \rightarrow 0$ and $\mathbf{J} \rightarrow 0$) reduces the right side of the equation to zero, which produces the more familiar form of the wave equation:

$$\nabla^2 \mathbf{E} - \mu_0 \epsilon_0 \frac{\partial^2 \mathbf{E}}{\partial t^2} = 0. \quad (1.11)$$

Assuming a solution contain harmonic time dependence, $e^{-i\omega t}$, and that the medium is isotropic and homogeneous, the Helmholtz Equation is obtained:

$$(\nabla^2 + k^2)\mathbf{E} = 0, \quad (1.12)$$

where k is the wavenumber given by:

$$k^2 = \mu \epsilon \omega^2, \quad (1.13)$$

where μ is the permeability, ϵ is the permittivity, and ω is the angular frequency. The Helmholtz equation prepares us to find the Green's function.

1.4 Green's Function

The Green's function is the impulse response of an inhomogeneous differential equation with specified boundary conditions. The scalar Green's function for the Helmholtz equation in two dimensions free space is:

$$G(\mathbf{x}, \mathbf{x}') = \frac{i}{4} H_0^{(1)}(k|\mathbf{x} - \mathbf{x}'|), \quad (1.14)$$

where the primed coordinates are the source points, the unprimed coordinates are the observation points and $H_0^{(1)}$ is a Hankel function of the first kind. This Green's function relates the induced currents on the surface of the mirror to the electric field in all space. The scalar Green's function in integral form is given by the following:

$$E(\mathbf{x}) = \int J(\mathbf{x}') G(\mathbf{x}, \mathbf{x}'), \quad (1.15)$$

where $J(\mathbf{x}')$ is the induced current on the surface, $G(\mathbf{x}, \mathbf{x}')$ is the aforementioned Green's function and, $E(\mathbf{x})$ is the observed electric field. The goal is to use the Green's function to calculate the currents on the surface. To simplify this calculation, a perfectly conducting surface is used.

1.5 Perfect Conductor

Applying the boundary conditions for the case of a perfect conductor greatly simplifies the problem of calculating the scattered wave to satisfy the Green's function. Using Eq. 1.15, the relationship for a perfectly conducting surface is shown. Focusing solely on scalar fields the total field, E_{tot} , is a superposition of the incident electric field, E_{inc} , and the outgoing scattered field, E_{out} :

$$E_{\text{tot}} = E_{\text{inc}} + E_{\text{out}}. \quad (1.16)$$

The total electric field on the surface on a conductor is zero. Focusing only on the conductive surface reduces Eq. 1.16 to

$$0 = E_{\text{inc}} + E_{\text{out}}. \quad (1.17)$$

Applying the Green's function to the scatter wave's electric field by applying Eq. 1.15 gives

$$E_{\text{out}}(\mathbf{x}) = \int J(\mathbf{x}')G(\mathbf{x}, \mathbf{x}')d\mathbf{x}'. \quad (1.18)$$

Substituting Eq. 1.18 into Eq. 1.17 lead to

$$0 = E_{\text{inc}}(\mathbf{x}) + \int J(\mathbf{x}')G(\mathbf{x}, \mathbf{x}')d\mathbf{x}', \quad (1.19)$$

which can be simplified to

$$E_{\text{inc}}(\mathbf{x}) = - \int J(\mathbf{x}')G(\mathbf{x}, \mathbf{x}')d\mathbf{x}'. \quad (1.20)$$

Now that the integral equation is formed the next step is to solve for the surface current, $J(\mathbf{x}')$. The surface current is used to calculate the electric field for all space. Solving for $J(\mathbf{x}')$ cannot be done using conventional algebra because it is within an integral. Linear algebra and forming a matrix equation leads to a solution for $J(\mathbf{x}')$.

1.6 Matrix Equation

The resulting integral equation (Eq. 1.20) is modeled as a matrix equation to solve for $J(\mathbf{x}')$.

Taking Eq. 1.20 and specifying the bounds of the integral across the surface of the mirror yields

$$E(\mathbf{x}) = \oint G(\mathbf{x}, \mathbf{x}')J(\mathbf{x}')d\mathbf{x}' \quad (1.21)$$

where the updated Greene's function, $G(\mathbf{x}, \mathbf{x}')$, is given in 1.14. The integral is then discretized across the surface of the mirror using numerical integration. The resulting equation is a sum of discrete current contributions across the surface shown by the following

$$E(\mathbf{x}) = \sum_j G(\mathbf{x}, x_j)w(x_j)J(x_j), \quad (1.22)$$

where the subscript j are the discretized points on the surface of the mirror and the function $w(x_j)$ is the general weighting function for whichever quadrature rule is used. Nystrom [8] Integration

is used to line up the region of observation (\mathbf{x}) with the discretized points across the surface(x_j). This provides discrete points of observation in the same locations as the current contributions in the summation from 1.22. This gives

$$E(x_i) = \sum_j G(x_i, x_j)w(x_j)J(x_j), \quad (1.23)$$

where the subscript i represent the observation point and the subscript j represent the source points across the surface of the mirror. Next, the following notation changes are made.

$$E(x_i) = E_i \quad (1.24)$$

$$G(x_i, x_j) = G_{ij} \quad (1.25)$$

$$J(x_j) = J_j \quad (1.26)$$

$$w(x_j) = w_j \quad (1.27)$$

The Green's function can be combined into a general function that will be called the impedance function, Z_{ij} . The following substitution demonstrates this simplification

$$Z_{i,j} = G_{ij}w_j. \quad (1.28)$$

This yields the following general equation

$$E_i = \sum_j Z_{ij}J_j, \quad (1.29)$$

where E_i represents the electric field produced from surface currents, J_j . This equation models a matrix equation with rows i 's and columns j 's. It is rewritten as spatial vectors E and J where each element represents the scalar values across the surface with a relationship matrix Z in the following manner,

$$E = ZJ. \quad (1.30)$$

The surface currents are then solved through inversion. Optimizing the solving process is taken more in depth in later chapters and is a focal part of this project.

1.7 Scope of Project

The purpose of this research is to take Johnson's [7] approach towards calculating surface currents and use it to analyze the scattering effects of an incident beam of light on a rough surface. The derived matrix equation (Eq. 1.30) is used as the foundation for this study. The FORTRAN computing language is used to generate surfaces of different roughness in both shape and depth and analyze the reflectance properties.

Limitations of Eq. 1.30 occur from inefficiencies in generating and solving for the surface current. Direct and iterative solutions are compared for accuracy and efficiency in this process. By optimizing the solving mechanism, more efficient results are realized and more realistic problem sizes can be used to model the effects of roughness from a two-dimensional conducting mirror.

The exploration of the multipole approximation is used to further optimization. Using the concepts of perturbation and linear algebra future work is proposed in how these simplifications will further the iterative solving approach. These approximations can provide faster calculations without loss of accuracy for given problem complexities.

Chapter 2

Numerical Methods/Setup

The project's model is broken in four parts. The model of the incident wave and its features comes first. Second, the modeled mirror is discretized and generated. The third element consists of constructing the matrix equation (Eq. 1.30) through the use of the two-dimensional Greene's function derived in the previous chapter. The final element of the project is calculating the far-field approximation of the scattered wave. The far-field approximation calculates the resultant scattering at different angles far enough away from the surface leaving only angular dependence. Fig. 2.1 depicts the interaction between all these elements.

2.1 Incident Wave

The incident wave is generalized to handle monochromatic light. The simplest two-dimensional wave is a uniform plane wave infinitely symmetric in one dimension. Generally a plane wave takes the form of

$$E_{\text{inc}} = E_0 e^{i\vec{k}\cdot\vec{r}} \quad (2.1)$$

where E_0 is the magnitude, \vec{k} is the wavenumber and \vec{r} is the direction of propagation. Fixing the problem to two-dimensions, the wave is contained in the x and y plane. Thus the wavenumber,

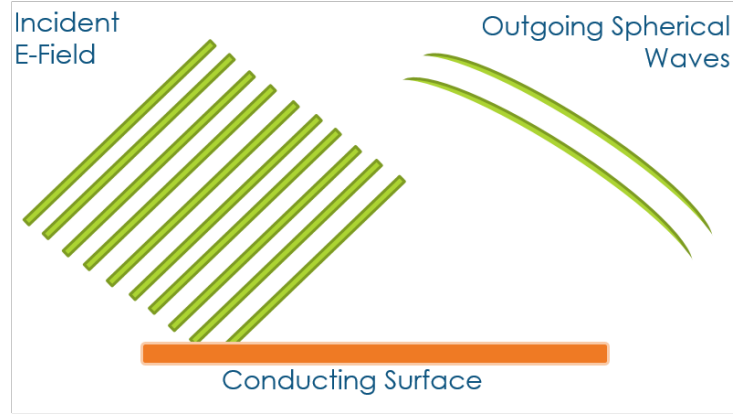


Figure 2.1 Setup of incident beam, outgoing spherical wave, and surface current Diagram.

\vec{k} , has an x component and a y component and is written

$$E_{\text{inc}} = E_0 e^{i(k_x x + k_y y)} \quad (2.2)$$

The variables for k_x and k_y are written in terms of the k value defined as $k = |\vec{k}|$, and the grazing angle θ such that Eq. 2.2 becomes

$$E_{\text{inc}} = E_0 e^{ik[x \cos(\theta) + y \sin(\theta)]} \quad (2.3)$$

In this project, the x direction is parallel to the surface in the noninfinite direction. The y direction is perpendicular to the surface and depicts the height from the surface. The mirror itself is contained in the x, z plane. The z direction is unused but symmetric to model a two-dimensional calculation and the positive z direction comes out of the page. Figure 2.2 shows the relationship between these directions and the surface as well as the representation of θ in the setup. For simple normalization, $tE_0 = 1$. For the incident wave, the y component is negative because the wave travels toward the surface. The incident electric field is thus given by

$$E_{\text{inc}} = e^{ik[x \cos(\theta) - y \sin(\theta)]} \quad (2.4)$$

With the incident wave modeled, the next step is to manipulate and model the surface itself.

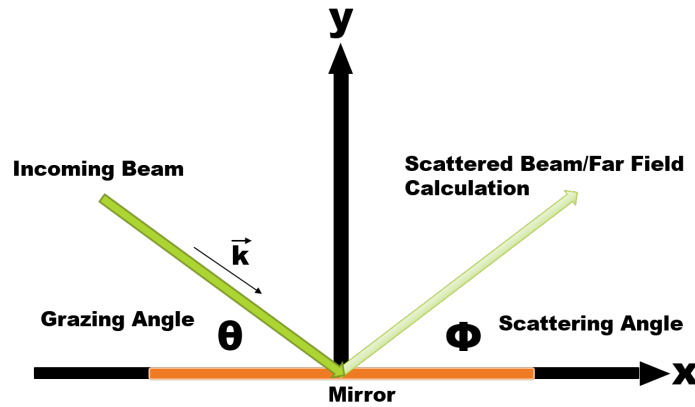


Figure 2.2 Orientation of coordinate system. The wavevector, \vec{k} , the grazing angle of the incident beam, θ , and the grazing angle of the scattered beam, ϕ , are shown. The x direction goes across the mirror, the y direction is perpendicular to the mirror, and the z direction is the unused infinitely symmetric direction and comes out of the page.

2.2 Surface Discretization

Numerical quadrature and discretization of the surface is discussed further, as mentioned, to show how 1.30 is utilized. In general, numerical integration is the process of changing continuous integrals into a discrete summations. This is represented by

$$\int f(x)dx = \sum_i c_i f(x_i) \quad (2.5)$$

where x_i represents discrete values at which the function is evaluated. The values c_i are the weighting coefficients that depend on the quadrature used.

2.2.1 Quadrature Rules

The more well-known quadrature rules consist of the rectangle and trapezoid methods. These rules use geometries of constant and linear order, respectively to discretize integrals which approximate the solution quickly but lacks the precision necessary for this project. Simpson's rule improves the order to the quadratic regime. In Fig. 2.3, the resulting precision of the summation improves as the

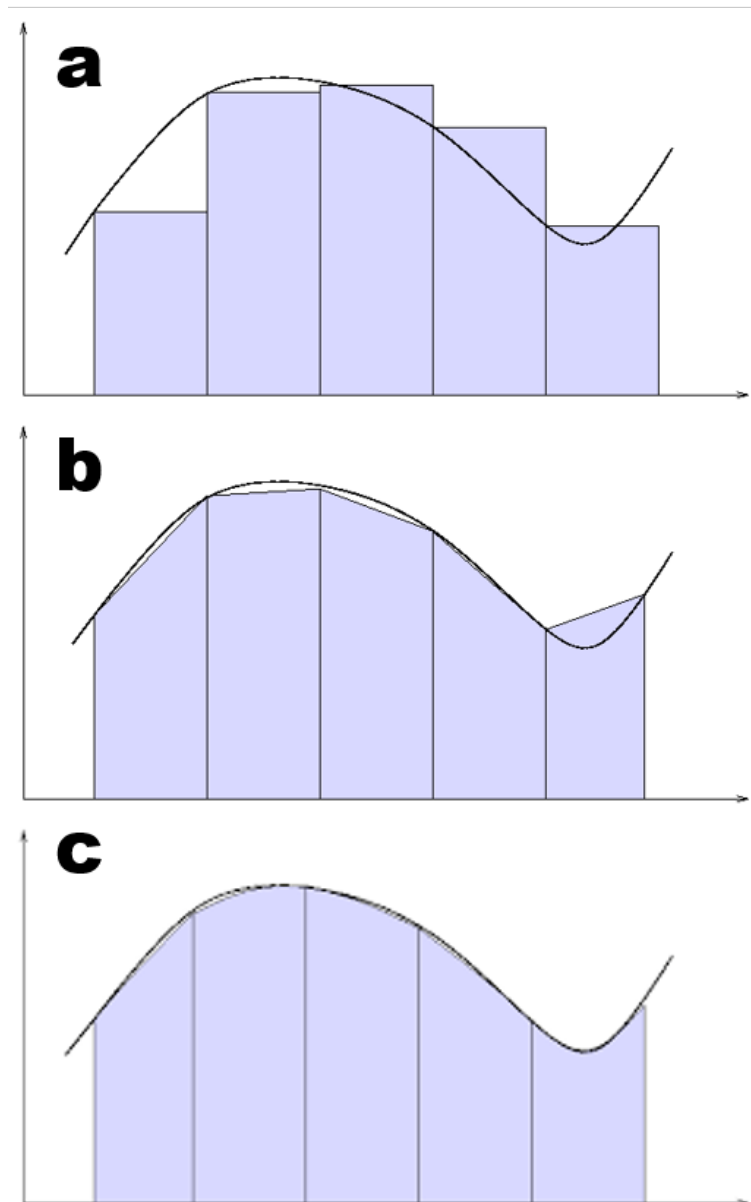


Figure 2.3 Common quadrature rules. Part *a* shows the zeroth order rectangular rule modeled by constant functions, *b* shows the first order trapezoid rule modeled by linear approximations, and *c* shows the second order Simpson's rule modeled by quadratic approximations [9]. The integral approximation is more accurate with higher-order methods.

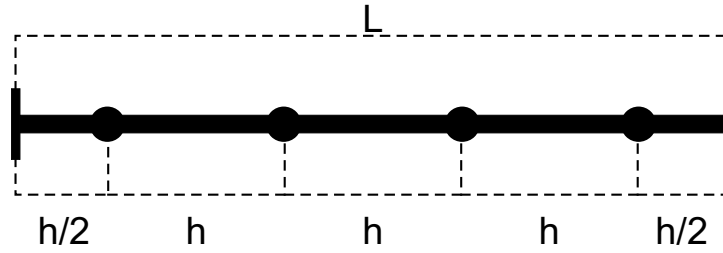


Figure 2.4 Cell-centered discretization of a patch divided into four discretized points. The distance L is the length of the patch, and h is the distance between discretized points.

order of the quadrature increases. The order reflect what type of function are used to approximate the integral. Fig. 2.3a shows the constant function approximation, b show the linear approximation, and c show the quadratic approximation. The quadratic is of the highest order depicted and the approximated blue region is closest to the actual function.

For this project, transforming the integral into a smooth summation poses a problem because of the precision required for a realistic result. The ideal rule is to employ a high-order quadrature rule. Higher-order quadrature rules are more precise because they converge to the exact answer quicker. The problem with higher-order rules is the need for a greater number of points.

To best handle and organize the quadrature points, a patch system is implemented, similar to the process of interpolation. As illustrated in Fig. 2.4, a patch contains four points that are equally spaced in the region. The length of a patch is given by L , and h is the distance between two discretized points within a patch. Thus, using a cell-centered approach the four quadrature points within a patch are located at $\frac{l}{8}, \frac{3l}{8}, \frac{5l}{8},$ and $\frac{7l}{8}$, and the area under the curve for a given patch is given by

$$A = c_1 f\left(\frac{l}{8}\right) + c_2 f\left(\frac{3l}{8}\right) + c_3 f\left(\frac{5l}{8}\right) + c_4 f\left(\frac{7l}{8}\right) \quad (2.6)$$

Johnson's thesis [7] provides the derivation for the weighting constants. His resultant derivation yields

$$c_1 = \frac{13l}{48} = \frac{13h}{12} \quad (2.7)$$

$$c_2 = \frac{11l}{48} = \frac{11h}{12} \quad (2.8)$$

$$c_3 = \frac{11l}{48} = \frac{11h}{12} \quad (2.9)$$

$$c_4 = \frac{13l}{48} = \frac{13h}{12} \quad (2.10)$$

With these constants a general summation formula can be used for most circumstances. A problem arises, however, when we attempt to use this method on a patch with a singularity.

2.2.2 Handling Singularities

When the patch contains a singularity, the above constants are insufficient in determining the value of the summation. Johnson provides a thorough derivation, but in this project the results are noted. To calculate the area under a singular function. The function is divided into the singular part, $\xi(x)$, and the remaining nonsingular part, $f(x)$.

$$\int_a^b \xi(x)f(x)dx = c_1f\left(\frac{l}{8}\right) + c_2f\left(\frac{3l}{8}\right) + c_3f\left(\frac{5l}{8}\right) + c_4f\left(\frac{7l}{8}\right) \quad (2.11)$$

where $\xi(x)$ contains the integrable singularity and the numerical constants are given by

$$c_1 = \frac{1}{6}[13.125W_0 - 17.75W_1 + 7.5W_2 - W_3] \quad (2.12)$$

$$c_2 = \frac{1}{2}[-4.375W_0 + 11.75W_1 - 6.5W_2 + W_3] \quad (2.13)$$

$$c_3 = \frac{1}{2}[2.625W_0 - 7.75W_1 + 5.5W_2 - W_3] \quad (2.14)$$

$$c_4 = \frac{1}{6}[-1.875W_0 + 5.75W_1 - 4.5W_2 + W_3] \quad (2.15)$$

The W_n are given by

$$W_n = \frac{1}{h^n} \int_a^b x^n \xi(x) dx, \quad (2.16)$$

with $n = 0, 1, 2, 3$. The derived quadrature rules can now be applied to flat surfaces.

2.3 Path Integrals

The mirrors modeled in this project are not flat but contain contours, thus the above integrals must be enhanced to integrate over the surface which isn't one-dimensional. A typical method for overcoming this problem is to integrate over the surface using a path integral depicted by

$$\int_C f(x)dx. \quad (2.17)$$

The summations modeled in the prior section are insufficient in handling two dimensions. However, a two-dimensional integral can be performed over one variable by incorporating the length of the path. The length of the path is found through the Pythagorean Theorem with differentials written in the following manner

$$\int_C f(x,y)\sqrt{dx^2 + dy^2}, \quad (2.18)$$

where dx and dy show the change in x and y across the surface at which values of the function $f(x,y)$ are evaluated. This integral can be solved through the fundamentals of calculus by multiplying a $\frac{dx}{dx}$ in the back and moving the denominator under the radical. Thus the path integral can be written as a one-dimensional integral:

$$\int_a^b f(x,y)\sqrt{1 + \left(\frac{dy}{dx}\right)^2}dx, \quad (2.19)$$

where the bounds a and b are starting and ending values of x , respectively. This numerical integration framework now allows us to discretize the surface over contours.

2.4 Generating the Matrix

With the discretization framework intact, the two-dimensional matrix eq can be filled. The matrix equation is modeled by the following summation. (see sec 1.6 for derivation)

$$E(x_i) = \sum_j G(x_i, x_j)w(x_j)J(x_j) \quad (2.20)$$

where x_j represents the source points, and x_i represents the observation points. Combining Eq. 2.20 with Eq. 1.30 the exact matrix generation function is show. Generating the matrix has two parts, the singular and nonsingular patches. Singularities arise when calculating the electric field at the location of the discretized surface current. These situations are found on the diagonal patches of the matrix. Thus, the diagonal patches are calculated using the singular constants (Eqs. 2.12, 2.13, 2.14, 2.15, and 2.16) mentioned in earlier section of this chapter and the off diagonal patches are calculated with the nonsingular constants (Eqs. 2.7, 2.8, 2.9, and 2.10). Each element of the impedance matrix, Z , (see Eq. 1.30) is generated with the following formula

$$Z_{i,j} = c_n \left[\frac{1}{4} Y_0(k_r) - \frac{i}{4} J_0(k_r) \right] \sqrt{1 + \left(\frac{dy}{dx} \right)^2}, \quad (2.21)$$

where

$$k_r = k \sqrt{(x_i - x_j)^2 + (y_i - y_j)^2}, \quad (2.22)$$

and c_n is the numerical constant from the quadrature rule. After filling the next step is to model the surface.

2.5 Surface Generation

Generating the surface contains two main parts, creating discretized values and splicing them together. Each point on the surface is given an x value representing its location across the surface and a corresponding y value that show the height of the surface at the location. Different surfaces can be generated simply by altering the heights (y) across the surface. These discrete points are then spliced together using splines of cubic polynomial order. These splines take a few points at a time and fits the data. This is done across the surface and each function is patched together similar to a piece-wise function. Now the surface model is continuous and better represents a real surface.

The first two surfaces generated were a flat surface and a linear surface of constant slope. Figure 2.5 shows representations of the surface under these conditions. The flat surface (Fig. 2.5a)

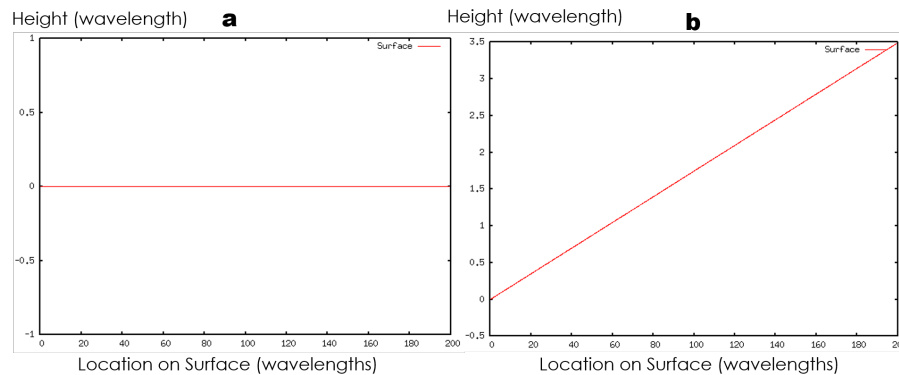


Figure 2.5 Surface generation of flat and linear surfaces. The graph on the left (*a*) shows the flat surface and the graph on the right (*b*) shows the linear surface for a given incline angle.

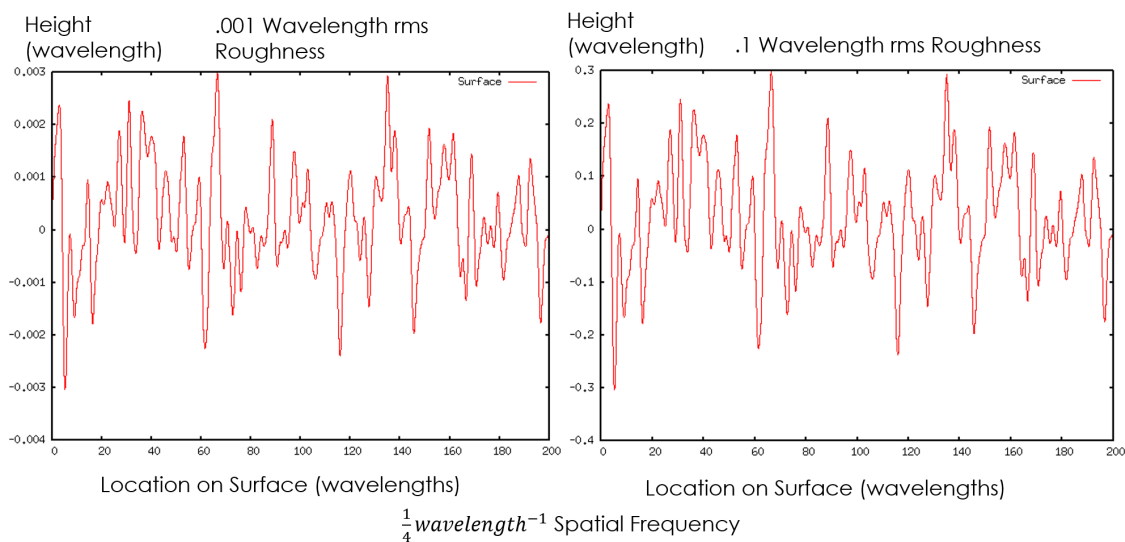


Figure 2.6 Two different surfaces generated with different rms roughness. The surfaces have the same spatial frequency and have a surface length of 200 wavelengths. The surfaces are practically identical except for the heights are different which can be seen by the scales of the y-axis

simulates the effects of a smooth surface without roughness, or the ideal surface. The constant slope (Fig. 2.5b) is also void of roughness and can be used as the ideal case to compare against different generated surfaces of varying roughness. As seen in the figure there is no roughness or noise across the surface modeling an ideal mirror.

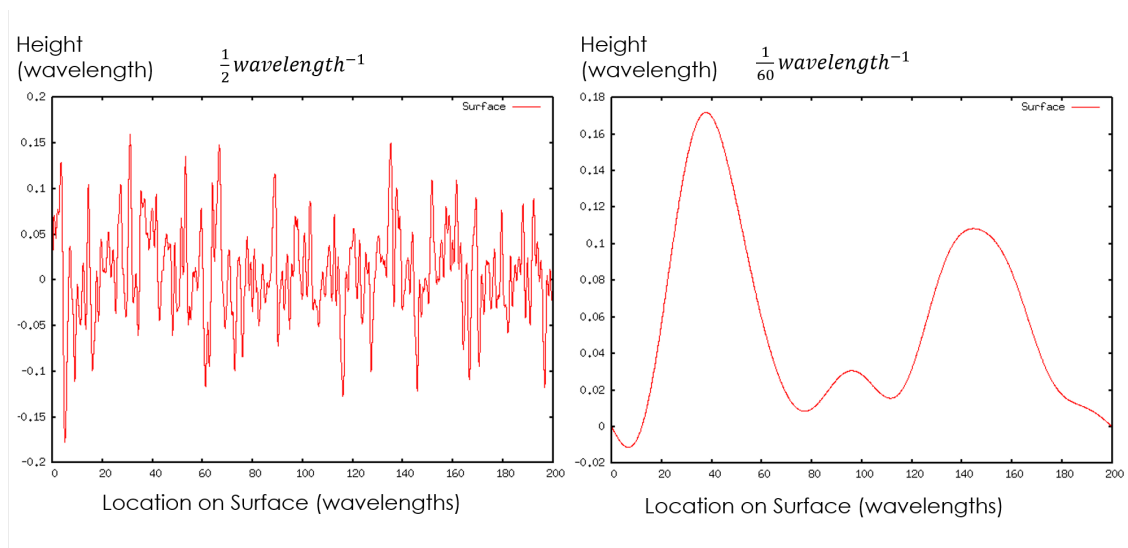


Figure 2.7 Two different surfaces generated with different spatial frequencies. The surfaces have the same rms roughness and have a surface length of 200 wavelengths.

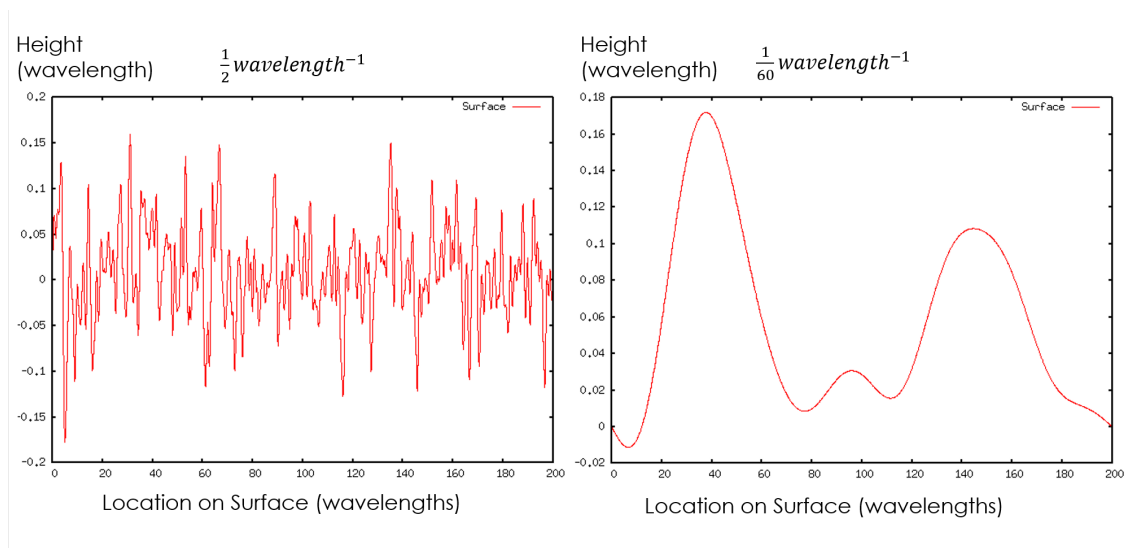


Figure 2.8 Two different surfaces generated with different spatial frequencies. The surfaces have the same rms roughness and have a surface length of 200 wavelengths.

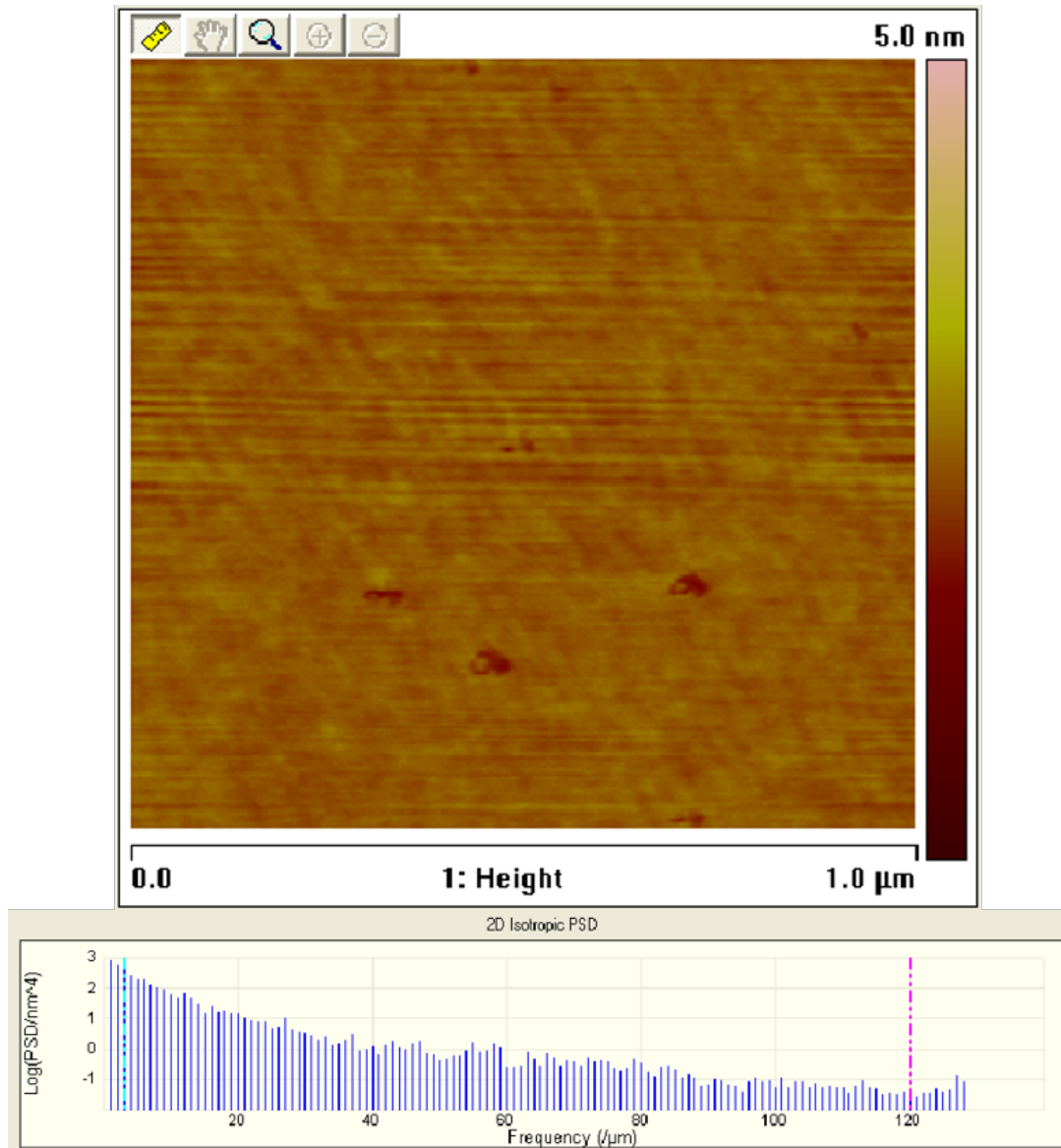


Figure 2.9 A mirror used in the lab used for extreme ultraviolet reflectance along with the power spectrum. The power spectrum shows discrete frequencies across the surface. The overall spectrum is similar in shape to a Gaussian.

A more realistic surface is random in nature. However, picking a random seed and generating random values for the y vector falls short of modeling realistic surfaces. A power spectral density of an actual mirror designed by the research group is give in Figure 2.9. This diagram shows the frequency spectrum of the surface of the mirror. The figure show that discrete frequencies are good models for matching the structure of real mirrors. Thus to model these mirror more realistically, two parameters will be considered, mean height and spatial frequency. To do this we begin with a frequency vector generated from random numbers. This vector is run through a high pass filter to eliminate the low, unrealistic, frequencies. Then, by taking a Fourier transform a random surface is generated with random frequencies rather than random values. Two surfaces are given in Fig. 2.6 of varying rms roughness. The graph on the left show 0.001λ rms roughness and the one on the right shows $.01\lambda$ rms roughness. The shape of the surface is practically unchanged except for the y scale on the graph shows thicker average roughness. These values were chosen because the resemble typical roughness found on actual mirrors. Altering the spatial frequency is represented in Fig. 2.8. The graph on the left shows high spatial frequency while the graph on the right shows small spatial frequency. Notice the rms high in both cases in the same however the number of bumps per length across the surface is much smaller in the graph on the right than on the one on the left. These two parameters will be tested for their effects on roughness.

2.6 Solving the Matrix Equation

Solving the matrix equation efficiently poses a challenge due to memory requirements and timing due mostly from the size of the problem. To map the surface with realistic precision, we hypothesize that a surface needs around 10^6 discretized points. This yields $10^6 \cdot 10^6 = 10^{12}$ elements in the impedance matrix. Using complex, double precision numbers of 16 bytes each, to store the matrix requires 16 Terabytes of memory. For the proof of principle of this project, the surfaces used in

this project were the most a four processor server could solve efficiently. Due to the immense size of the matrix the solving process of the problem need be efficient in both timing and memory. To do this we explored two types of methods, direct and iterative solvers.

Direct matrix solver provide easy-to-code solutions but are costly in both memory and computational time. Direct methods such as inversion and lower upper decomposition (LUD) [10] are very costly but given enough time solve the problem directly. Most optimized routines provide a "Big Oh" [11] notation of n^3 , which is computationally expensive for the task it is to perform. Another big downside to LUD is difficulty of parallelizing the code. The process requires all the information be accessed and operated on at the same computational location restricting it to one processor. Due to these disadvantages, another approach was sought.

Iterative solvers are more complicated to code but can cut time on memory and computation time. Iterative solver depend on a well conditioned initial guess that is multiplied and compared against the actual matrix product. The desired vector is then altered and multiplied again. This is repeated until the vector is within the desired precision allowing for major speedup due to a couple of key elements in this project. First, the flat surface can be calculated quickly and can be used as a very good initial guess towards finding the effects of roughness. Second, surface roughness can be viewed as a perturbation from the smooth case. The solver would take the smooth surface and used perturbative corrections until within the range of precision. This provides a speedup by exiting the program earlier which is more optimal than a direct method searching for exact answers. The "Big Oh" notation for these methods are $n^2 \log(n)$. The iterative solver utilized in this program was the general minimal residual method [12] (GMRES).

2.7 Far-Field Calculation

The effects of roughness are obtained through a far-field calculation of the scattered wave. When the scattered beam is "far-enough" away from the beam the radial dependence is much smaller than the angular dependence of the electric field. Johnson [7] provides a detailed derivation for a far-field approximation. Applying his equation to this project's parameters yields

$$E(\phi) = \int_C J(x', y') e^{-ik(\cos(\phi)x' + \sin(\phi)y')} ds', \quad (2.23)$$

where ϕ is the observation angle measured from grazing as see in Fig. 2.2. This equation is used to calculate the result for multiple observation angles, ϕ , to analyze the scattering of the wave. The far-field calculation is then used to determine overall reflectance and reveal relative extrema in the reflectance at angles away from the incident grazing angle. This calculation thus reveals the relative effect surface roughness has on the intensity of scattered wave at different observed angles. The far-field calculation of the scattered electric field for a flat surface is given in Fig. 2.10. This flat surface calculation is used as the baseline result to identify the effects of altering the rms roughness and spatial frequency of the mirror.

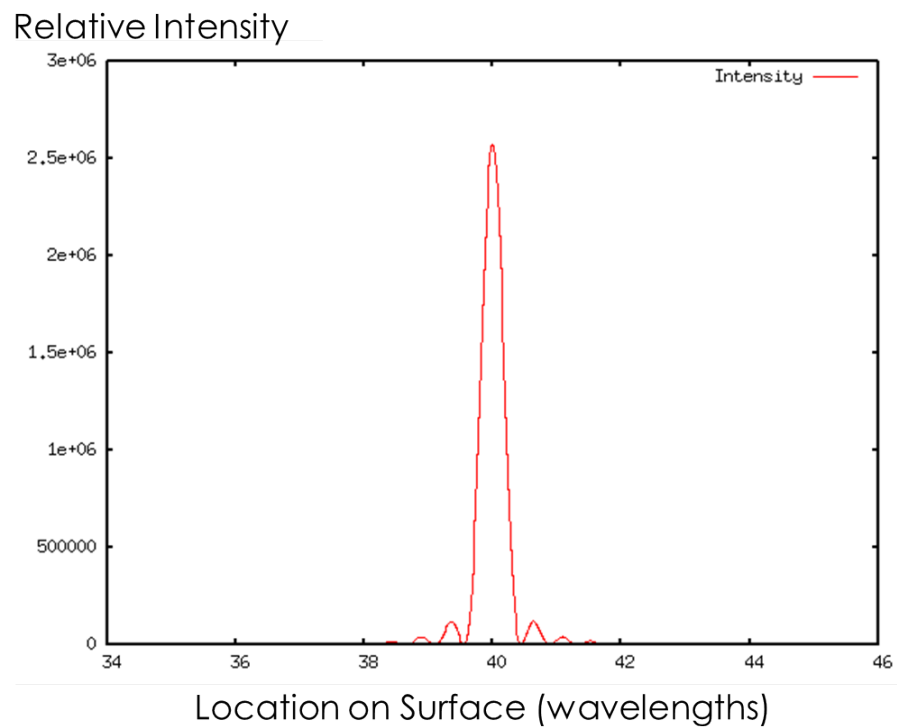


Figure 2.10 The effects reflection of 40 Degree grazing angle on a flat surface 200 wavelengths long. The main peak is matches the incident as the law of reflection suggest. The secondary peak suggests scattering even for a flat surface.

Chapter 3

Results

Reflectance calculations are given for randomly generated surfaces. Two key surface parameters are adjusted to show their overall effect on roughness (see Sec. 2.5), namely, rms roughness and spatial frequency. The optimization of the solving process is given through the speed-up from transitioning from LUD to GMRES. Relative computational times for filling and solving the matrix equation are given for different sized problems.

3.1 Effects of surface roughness

The process to create the surface takes in two key parameters, rms roughness and spatial frequency. When studying the effects of one the other is held constant to isolate the influence of one independently. The rms roughness is the root mean square of the height and acts like the surface is being stretched. The spatial frequency is the number of completed period per wavelength across the mirror.

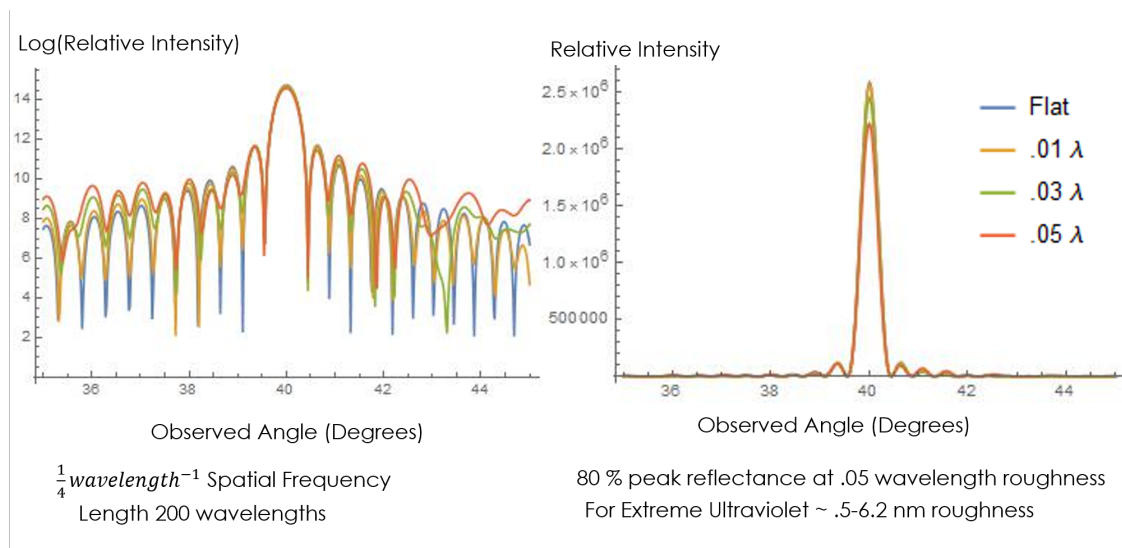


Figure 3.1 Reflection from different rms roughness of an incident beam of grazing angle 40 Degrees. Each surface has same surface length and spatial frequency as labeled in the figure. The left graph shows a Logarithmic plot of the intensity and the right show the unaltered intensity.

3.1.1 rms Roughness

The program model described in chapter 2 is used to generate multiple surfaces of varying rms roughness. The differing rms roughness can be seen in Fig. 2.6. Looking at this figure, you can see in both cases the surface shape looks almost entirely the same. The y-axis scaling shows that the surface on the right has greater rms height. For these graphs, the length of the mirror was chosen to be 200 wavelengths because it approaches the maximum number of points that can be used efficiently on a lab computer. Longer mirrors that better model realistic surfaces can be analyzed using higher memory machines as is outlined in the optimization section of the chapter.

As seen in Fig. 3.1, the effects of rms roughness have a direct impact on the reflectance. The roughness used in these graphs ranges from 0.01λ to 0.05λ . Figure 3.1a displays the log of the reflectance of the different outgoing angles and Fig. 3.1b resembles the raw observed intensity. In both graphs the spatial frequency was held constant at $\frac{1}{4}\lambda^{-1}$ and the incident angle was chosen to be 40 Degrees. These graphs show that at 0.03λ the intensity of the main peak loses about 10%,

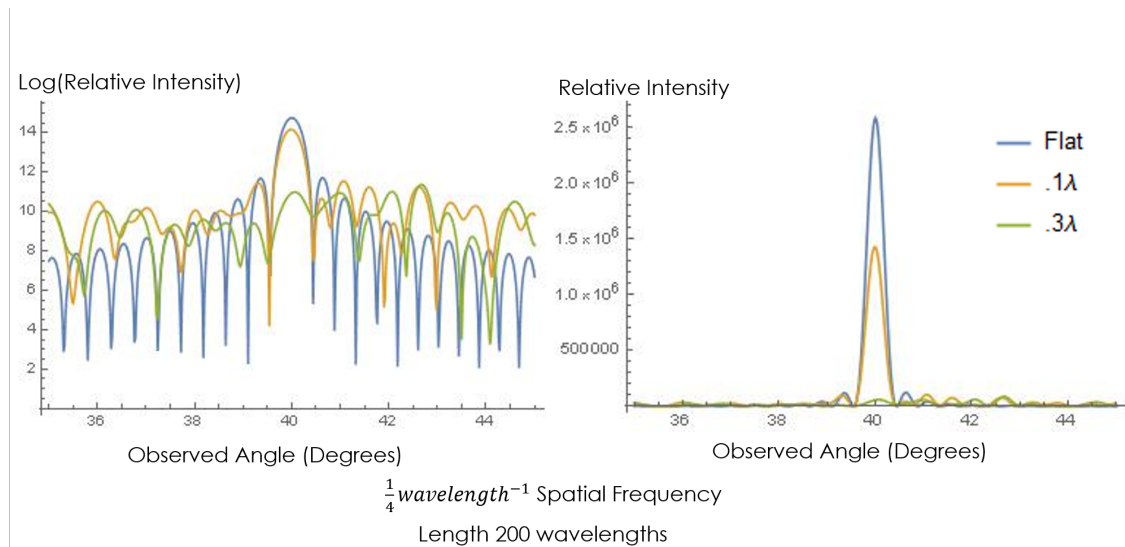


Figure 3.2 Reflection from different extreme rms roughness of an incident beam of grazing angle 40 Degrees. Each surface has same surface length and spatial frequency as labeled in the figure. The left graph shows a Logarithmic plot of the intensity and the right show the unaltered intensity.

and as the rms roughness reaches 0.05λ , the peak reflectance is reduced by 20%. Looking at the logarithmic plot on the left, as the rms roughness increased the secondary peaks gained intensity. Thus, as the main peak reflectance decreases, light is not lost but simply scattered at different angles.

Increasing the rms roughness to more extreme cases led to intriguing results. As seen in Fig. 3.2, surfaces are generated with roughness of 0.1λ and 0.3λ . The graph show the decrease in peak reflectance in each case. With 0.1λ rms roughness, the peak reflectance was reduced by 40% and at $.3\lambda$, the peak reflectance was reduced by more than 98%. Thus, with these extreme levels

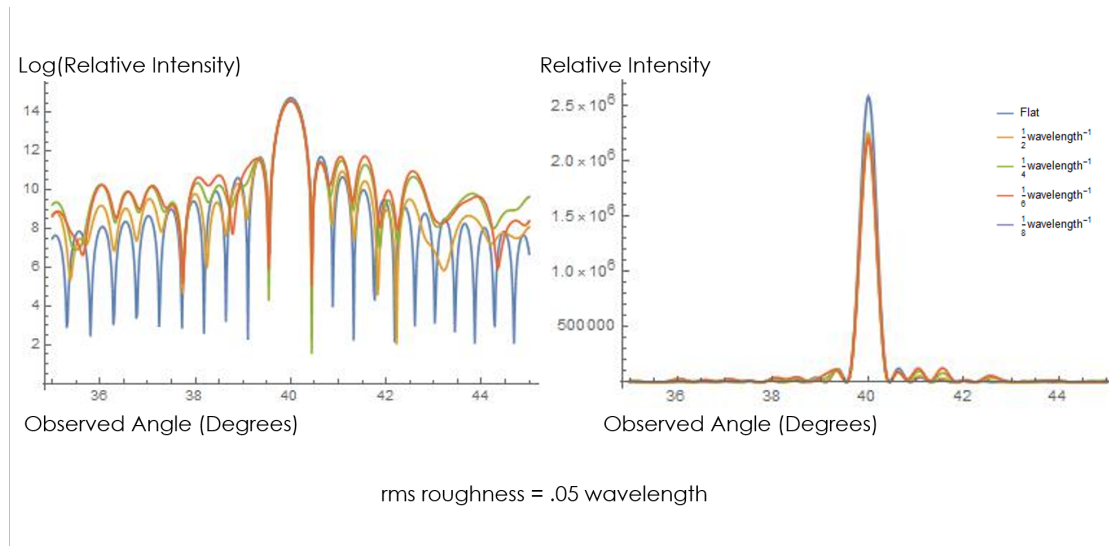


Figure 3.3 Reflection from different spatial frequencies of an incident beam of grazing angle 40 Degrees. Each surface has same surface length and rms roughness as labeled in the figure. The left graph shows a Logarithmic plot of the intensity and the right show the unaltered intensity.

of roughness, the reflection drops off quickly.

3.1.2 Spatial Frequency

The spatial frequency of the surface is a parameter to used determine it effects on reflectance. The effects of altering the spatial frequency can be seen in Fig. 2.8. These graphs are taken with surface length of 200 wavelengths and an incident angle of 40 Degrees.

The reflection from altering spatial frequency has a similar effect as rms roughness. Figure ??

shows that as the spatial frequency decreases the peak reflectance likewise decreased. In the graph on the left the secondary peak increased which shows that light was not lost but simply scattered to further angles. Thus, greater spatial frequency minimizes the effects of roughness for a given rms roughness.

3.2 Optimization

A major struggle in these reflectance calculations is the rate at which the program produces results. The strain is mostly due with finding the surface current through filling and solving the matrix equation (see 1.30). In this section, the solving times for different problems are given and the iterative method is shown to be more efficient than the direct solver. The newly optimized solve time is compared against the fill time. The fill time is broken down into singular and nonsingular portions and their relative time contributions are provided.

3.3 Direct vs iterative

The matrix equation (Eq. 1.30) was solved using direct and iterative techniques to show the advantages. Direct solutions are much easier to code, however, due to the nature of the problem, iterative solutions provided a much improved efficiency. The optimal direct solver used was lower upper decomposition (LUD) and the optimal iterative solve was the general minimal residual method (GMRES). The timing of each is taken for different sized surfaces. Figure 3.4 shows a log plot of the runtimes with a linear regression given for each case. The slope of LUD was 2.966 and for GMRES 2.36. These slopes show how LUD is $O(n^3)$ and GMRES is $O(n^2 \log n)$. Thus, the iterative solver is more efficient for this project.

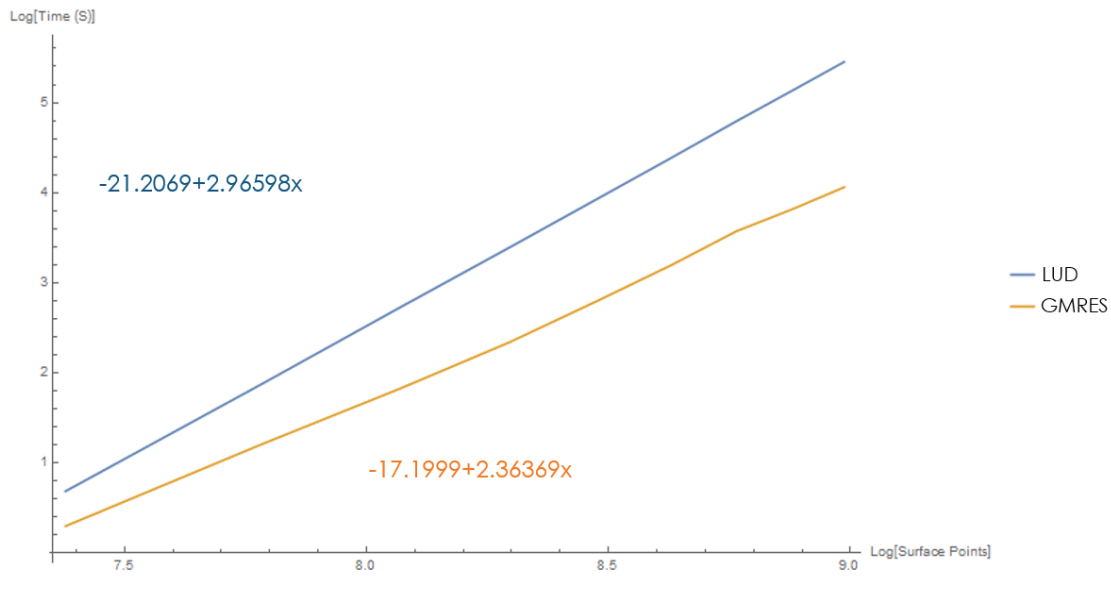


Figure 3.4 Results from running calculation of different surface lengths under different solving techniques. The equation represents the linear fit for the log plot. Lower upper decomposition (LUD) is a direct method and general minimal residual method (GMRES) is an iterative technique.

3.4 Fill vs solve

Times to fill the matrix are broken down into two parts the singular patches and the nonsingular patches. The program is run for different sized surface lengths on same seeded random surface with the iterative solver. The results are given in Table 3.1. The table suggests the nonsingular fill time is much larger than the singular time and the solve time. This piece of data is further discussed in the next chapter on how it can be improved.

Table 3.1 Comparison of the computational times for different processes in the reflection calculation. The majority of the computational time is found in the solving portion. The fill time is monopolized by the nonsingular patches of the matrix.

Surface length (wavelengths)	Non-singular Fill (s)	Singular Fill (s)	Total Fill (s)	Solve Time (s)
200	0.928	0.076	1.008	1.34
500	6.084	.228	6.312	10.364
1000	25.332	0.412	25.756	59.816
1250	45.376	.496	45.892	93.068
1500	61.956	0.66	62.62	150.612

Chapter 4

Conclusions and future work

I propose a threshold that defines the range of roughness whose effects on reflection are so significant they can't be ignored. Reflection calculations from randomly generated mirrors compare well with the conclusions made by Debye-Waller. The effects of reflection from spatial frequency contrast with prior work, specifically, the work of Stearn. A method known as the multipole approximation is explained and theorized to combat the slow timing of the matrix generation stage of the calculation.

4.1 Roughness threshold

The effects of rms roughness are provided by Fig. 3.1. Using the flat surface as a baseline comparison, the magnitude of the peak shows the loss of reflection due to increasing rms roughness. The curve showing 0.01λ depicts a subtle alteration to the peak reflectance. After increasing the roughness to 0.05λ , a greater dip in peak reflectance is seen. The loss of peak reflectance at this wavelength hangs around 20%, which is quite substantial in most experiments. Thus, the threshold where roughness effects are seen falls between 0.01λ to 0.05λ .

In extreme rms roughness situations as depicted in Fig. 3.2, there is a threshold in which all

materials lose the ability to reflect. The figure shows that at 0.1λ there is a loss of reflection close to 50%. Taking the roughness further to 0.3λ scatters nearly all of the incoming beam. Thus, the threshold when a material loses the majority of its reflectance, diminishing their mirror-like properties, occurs on the range of rms roughness between 0.1λ to 0.3λ

4.2 Comparison to Debye-Waller

Collecting reflectance data over multiple incident angles and rms roughness of randomly generated surfaces provides a comparison to the Debye-Waller (DW) correction factor. The DW correction factor (Eq. 1.2) proposes the key characteristic of surface roughness is the qh value. This value is comprised of the perpendicular moment transfer, q , and the rms roughness height, h . To make an effective comparison, the qh value is used as the plotting parameter. The results are found in Fig. 4.1.

Figure 4.1 provides insight into the accuracy of the DW correction factor. The organized clustering of the data suggest the qh value is an accurate parameter to characterize mirrors. The data was generated using random incident angles and rms roughness but all seem to follow according to the qh value. My data supports the accuracy of the qh value as a defining characteristic of the effects of roughness. The DW model matches the data at small values of qh , however, as qh increase the model deviates from the data. The error bars suggest greater variance as qh increases.

Fitting the experimental data suggests additional correction terms beyond the quadratic. The DW correction factor solely uses the quadratic term to model reflectance. The weighted fit of our data suggests the following correction:

$$R = R_0 e^{\alpha qh + \beta q^2 h^2 + \gamma q^3 h^3} \quad (4.1)$$

where

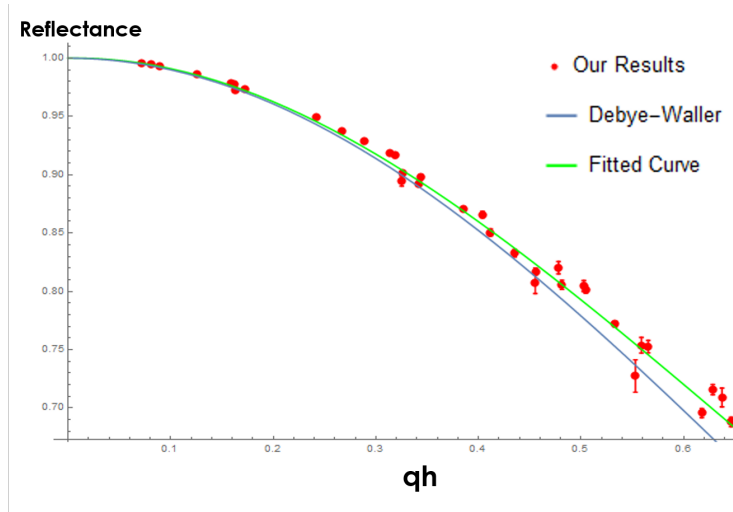


Figure 4.1 Comparison of data to Debye-Waller correction factor. The qh value is the momentum transfer multiplied by the rms roughness height. Random height and incident angles were chosen and the resulting reflectance is recorded. The data is fitted using a linear model and the equation is given in Eq. 4.1.

$$\alpha = .0146 \pm .0046, \quad (4.2)$$

$$\beta = -1.06 \pm .0464, \quad (4.3)$$

$$\gamma = .223 \pm .0944 \quad (4.4)$$

The values of α , β , and γ represent the linear, quadratic, and cubic terms respectively. The DW model proposes the quadratic term is the sole contributor to roughness. The value of the quadratic term of the DW correction factor is negative one. My model supports DW in the precision of the quadratic term especially since the error is small relative to the parameter value. The linear and cubic terms in my fit help account for the data at higher qh values. In the absence of these two terms the precision falls off quickly as the qh value increases suggesting that more terms are needed to model the effects of reflectance. The relative small errors of all three terms validate their contribution.

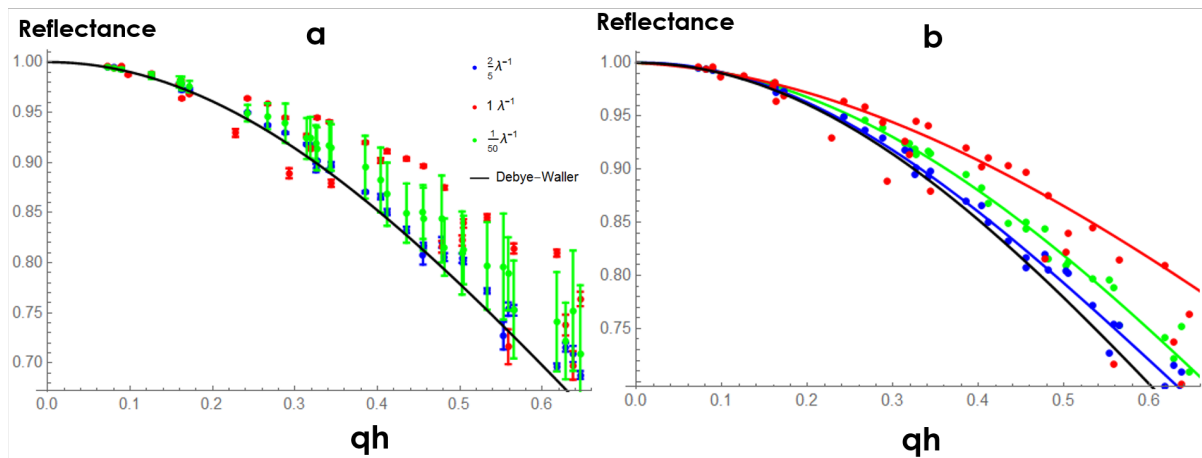


Figure 4.2 Reflectance calculations from three different spatial frequencies. The error bar(a) and the fits(b) are depicted for the same set of data. The Debye-Waller correction is also plotted for comparison. The spacing between fit lines suggest spatial frequency is an important parameter to consider in determining reflectance from roughness

4.3 Spatial frequency implications

Collecting similar data for different spatial frequencies reveals its contribution as a parameter to characterize surfaces. Figure 3.3 shows a change in peak reflectance as the spatial frequency is adjusted. Figure 4.2 shows the results of calculating reflectance from three different spatial frequencies, $\frac{2}{5}\lambda^{-1}$, $1\lambda^{-1}$, and $\frac{1}{50}\lambda^{-1}$. The incident angle and rms roughness height was also adjusted to provide a range of qh values.

Figure 4.2a shows the error bars of the data points and 4.2b depicts the fits for each frequency. The $\frac{1}{50}\lambda^{-1}$ is the low frequency extreme case. The error bars of this frequency are relatively large. This suggests an increase in variance as the frequency decreases. The $1\lambda^{-1}$ frequency, on the contrary, is the high frequency extreme. The error bars in this case are relatively small thus suggesting minimal variance. The fit lines in Fig. 4.2b depict the effects of adjusting the spatial frequency, and the disparity in each curve emphasizes the accuracy of spatial frequency as a surface characteristic.

The spatial frequency results show there are more parameters besides rms roughness that affect reflection. Thus, correction factors like DW and others who similarly limit the included parameters in their correction fall short of accurately modeling the effects of roughness. Other current studies make similar assertions in developing proper correction factors. Stearn [13] used different geometries of similar rms roughness and found equivalent results. They propose the index of refraction, incident momentum, rms roughness, and spatial geometry of the surface all contribute in correcting for roughness. More specifically, they created a linear surface, an exponential surface, and a sinusoidal surface. The lower frequency distributions had the steepest trend lines which matches the results in Fig. 4.2. Thus, rms roughness is not the sole parameter to formulate an accurate correction factor.

4.4 Multipole expansion

The slow timing of the matrix generation stage in the calculation can be combatted through the use of the multipole moment approximation [14]. Table 3.1 shows that generating the nonsingular elements of the impedance matrix monopolized the computation time. The nonsingular portion of the calculation is comprised of all the off diagonal elements of the matrix. Equation 2.21 shows the relative size of each element. This information reveals the matrix will be diagonally dominant,

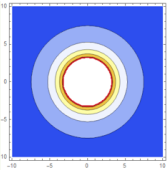
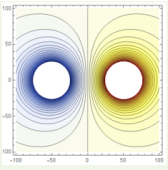
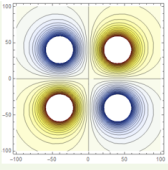
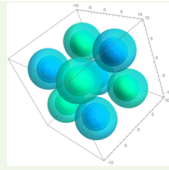
Pole	Monopole	Dipole	Quadrupole	Octupole
R- dependence	$\frac{1}{R}$	$\frac{1}{R^2}$	$\frac{1}{R^3}$	$\frac{1}{R^4}$
Diagram				

Figure 4.3 Each of the first four pole in the multipole are given. The spatial dependence is provided in the middle row, and a physical depiction of each is provided in the bottom row.

and each off-diagonal element will get progressively smaller the further they are from the diagonal. This is the ideal setup for the multipole expansion.

The multipole expansion takes the Green's function and expands it into a power series. Thus, each term in the series is a correction to the overall electric field. Figure 4.3 depicts each pole and corresponding radial dependence. Each term of this power series increases its radial dependence by a factor of $\frac{1}{r}$. The first few terms are named: monopole, dipole, quadrupole, and octupole. The elements of the impedance matrix can be modeled into poles to simplify the nonsingular fill time.

The slow computational time of the nonsingular fill is due to the immense amount of terms off the diagonal. The numbers of operations can be reduced by grouping terms of similar values together into poles. The elements close to the diagonal would be calculated directly and as you got further away from the diagonal less and less terms in the series would be needed to approximate the field to the desired precision, thus minimizing the number of calculations and reducing the fill time for the nonsingular elements.

Bibliography

- [1] P. W. Wachulak, A. Torrisi, A. Bartnik, L. Wegrzynski, T. Fok, and H. Fiedorowicz, “A desk-top extreme ultraviolet microscope based on a compact laser-plasma light source,” *Applied Physics B: Lasers and Optics* 123 (2017).
- [2] P. Naulleau, C. N. Anderson, W. Chao, K. A. Goldberg, E. Gullikson, F. Salmassi, and A. Wojdyla, “Ultrahigh efficiency EUV contact-hole printing with chromeless phase shift mask,” In *Proceedings of SPIE - The International Society for Optical Engineering*, 9984 (2016).
- [3] P. Debye, “Interference of Rontgen Rays and Heat Motion,” *Applied Physics* 15 (1913).
- [4] P. Croce and L. Nevot, *J. De Physique Appliquee* 11 (1976).
- [5] J. K. V. Holy and I. Ohlidal, *Physical Review B* 47 (1993).
- [6] B. P. L. Nevot and J. Corno, *Revue Phys. Appl.* 23 (1988).
- [7] J. Johnson, “Computationally Modeling the Effects of Surface Roughness on Soft X Ray Multilayer Reflectors,” *BYU Masters Thesis* (2006).
- [8] E. J. Nystrom, “Uber Die Praktische Auflosung von Integralgleichungen mit Anwendungen auf Randwertaufgaben,” *Acta Math.* **54**, 185–204 (1930).
- [9] J. Stewart, *Calculus*, 7 ed. (Cengage Learning EMEA, 2008), pp. 538–539.

-
- [10] J. R. Bunch and J. E. Hopcroft, “Triangular Factorization and Inversion by Fast Matrix Multiplication,” *Mathematics of Computation* **28**, 231–236 (1974).
- [11] S. Dasgupta, C. H. Papadimitriou, and U. Vazirani, *Algorithms*, 1 ed. (McGraw-Hill, Boston, 2008), pp. 6–8.
- [12] Y. Saad and M. H. Schultz, “Parallel direct methods for solving banded linear systems,” *Linear Algebra and Its Applications* **88-89**, 623–650 (1987).
- [13] D. G. Stearns, “Scattering of x rays from nonideal multilayer structures,” Technical report (1989) .
- [14] D. J. Griffiths, *Introduction to Electrodynamics*, 4 ed. (Pearson, Harlow, Essex, 2014), pp. 146–153.
- [15] L. de Physique des Lasers, “Multipole and Laser Excitation,” 2003.